POAC'25
St. John's, Newfoundland and Labrador, Canada

Proceedings of the 28th International Conference on Port and Ocean Engineering under Arctic Conditions
Jul 13-17, 2025
St. John's, Newfoundland and Labrador
Canada

Numerical simulation of installation of suction caisson for offshore wind turbine foundation

Lemuel Y. Thompson[1], Bipul C. Hawlader[2]
[1, 2]Memorial University of Newfoundland, St. John's, NL, Canada

ABSTRACT

Offshore wind energy is increasingly becoming an economical renewable energy source and has seen significant uptake in recent years. In Canada however, the offshore wind energy sector is yet to take off despite Atlantic Canada possessing one of the highest offshore wind resources in the world. This calls for research into design tools in the context of Canadian marine soils that will contribute to adopting offshore wind turbines (OWT) in Canada. This research performs a numerical analysis of the installation of OWT foundations.

The installation of OWTs is characterized by the large deformation of soils which cannot be captured by traditional Lagrangian finite element methods. The Coupled Eulerian Lagrangian (CEL) approach in Abaqus is capable of capturing large deformations and as such is adopted in this study. The modified Cam clay critical state model is implemented in a VUMAT interface and coupled with a hydromechanical code that allows for the computation of excess pore water pressures. This enables one to perform an effective stress based analysis as opposed to the widely used but limited total stress approach. This tool is then used to study the installation of suction caisson into glaciomarine sediments in the Bay of Fundy in Atlantic Canada. The distribution of effective and total radial stresses and excess pore water pressures in the soil during installation is studied to better understand the soil's response. With this, improved estimation of the penetration resistance during installation can be made.

KEYWORDS: Coupled Eulerian Lagrangian approach; Finite Element, Modified Cam Clay; Effective stress based analysis; Suction caisson

1 INTRODUCTION

Offshore wind projects have seen a sharp uptake in recent years as an efficient renewable energy source. By the end of 2022, the global installed capacity of offshore wind energy reached 59,009 MW with 8,385 MW of new commissions. Most of the growth in that year is attributable to China, which commissioned 5,719.6 MW in 2022 (Musial et al., 2023). As of 2024, Canada has no operating offshore wind turbines despite having significant potential for development (Blue & Jeyakumar, 2022).

The foundations for offshore wind turbines (OWTs) can largely be categorized into two groups: (a) fixed-bottom foundations, and (b) floating foundations. The fixed-bottom foundations have a solid continuous structure that extends from the seabed to the turbine. Floating OWTs use a buoyancy mechanism that enables the structure to float at the ocean surface with mooring lines anchored to the sea-bed (Tang & Kilpatrick, 2021). Fixed-bottom foundations are suitable for shallow water depths (< 60 m), and floating types are commonly used for deeper conditions. Currently, fixed-bottom OWTs are more common; however, higher offshore wind resource potential in deeper waters demands effective floating foundations.

1.1 OWT foundations

Figure 1 shows different OWT foundations with their corresponding water and embedment depths. For gravity-based foundation systems (Fig. 1a), the tower structure that protrudes above the water line is connected to a heavy mass, usually made of concrete or ballast-filled shell that simply rests on the seafloor (Kopp, 2010). Figure 1(b) shows the monopile foundation type. This is the most common foundation type—60.2% of the total existing global offshore wind energy projects (Musial et al., 2023). Monopiles are required to be stiff and rigid to be able to withstand the wind and tidal actions (Leblanc et al., 2010).

Figures 1(c–e) show the application of suction caissons for both fixed-bottom and floating OWT foundations. Suction caissons are relatively shorter, large-diameter cylinders with one end open. It can be used in groups, such as suction bucket jackets for wind turbine foundations, tripods or serve as anchors for tension-leg mooring lines for floating foundations (Fig. 1e). They can also be used individually, such as to support monopiles that connect to it at the seafloor and to anchor floating production storage and offloading (FPSO) unit (Fig. 1c). One major limitation to using suction buckets is the water depth as they restrict the amount of driving force available for installations (Houlsby & Byrne, 2005).

The generation, distribution, and dissipation of excess pore water pressure during installation not only affect the penetration resistance but also the pullout capacity of the suction caisson (Cao et al., 2002). Most of the available numerical studies simulated the penetration of piles and suction caissons in undrained conditions without calculating pore water pressure. In the present study, the penetration of a suction caisson is simulated by implementing the modified Cam clay model in Abaqus CEL. The simulations are performed for large deformations without mesh distortion.

1.2 Offshore wind resources in Atlantic Canada

Atlantic Canada possesses some of the highest-quality offshore wind resources. In a global review, areas around Eastern Nova Scotia and Newfoundland in Atlantic Canada were designated as one of the five regions worldwide considered to have strong wind power potential (Archer & Jacobson, 2005). Eamer et al. (2021) studied wind power densities at a height of 100 m above the sea surface

for Atlantic Canada and the US, where higher power densities were observed in Atlantic Canada, particularly around Nova Scotia and Newfoundland.

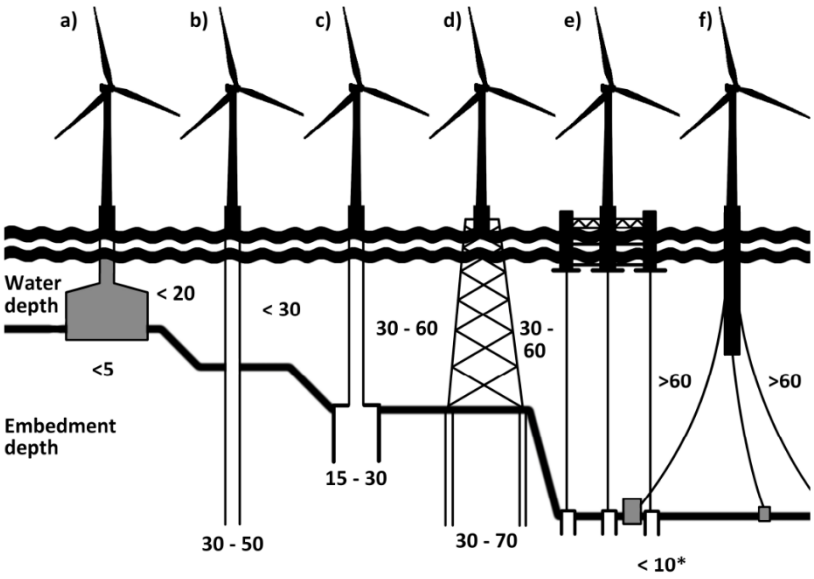

Figure 1. Fixed-bottom (a to d) and free-floating (e and f) OWT foundations with corresponding water and embedment depths. a) Gravity base, b) monopile, c) suction caisson, d) jacket (tripod has similar characteristics), e) semi-submersible floating with tension-leg mooring, f) floating–spar with catenary loose mooring (Eamer et al., 2021).

1.3 Geotechnical profile of marine soils in Atlantic Canada

The inner continental shelf of Atlantic Canada has surficial geology that resulted from repeated quaternary glaciations during the glacial period (Shaw et al., 2006). This event caused the deposition of glacial diamict (till) overlying the bedrock. Meltwater plumes from the retreating ice then deposited a drape of glaciomarine mud over the till (Eamer et al., 2020). During the post-glacial period, older glacial sediments in some areas, like the Northumberland Strait, were reworked as a result of changing relative sea levels. This generally resulted in a higher proportion of sand and gravel in these areas (Eamer et al., 2020). Currently, modern processes are accumulating post-glacial mud in sheltered basins and harbours, and post-glacial sand and gravel are being reworked in shallow areas where sea waves and currents are strong (Eamer et al., 2020).

Atlantic Canada marine soils can be classified largely as “soft” bedrock, “consolidated” sedimentary, till, glaciomarine mud, post-glacial mud or post-glacial sand and gravel (Eamer et al., 2020). Eamer et al. (2020) divided Atlantic Canada into 23 sub-regions, where within a given sub-region, the soils have similar properties. A summary description of the soil types is provided in Table 1 (for detailed distribution of different soil types in Atlantic Canada, see Eamer et al., 2020).

The choice of foundation type (fixed-bottom or floating) also depends on the type of soil at the site. Post-glacial sand and gravel is suitable for gravity foundations; glaciomarine and post-glacial mud are suitable for monopiles, jackets/tripod and suction caissons; and till is suitable for gravity

and floating foundations (Eamer et al., 2021). Till has very high shear strength; however, because of the boulder content, it presents a challenge to the installation of monopiles and suction caissons.

Table 1. Soil type description in Atlantic sub–regions (Eamer et al., 2020).

Predominant soil type	**Description**	**General properties**
Till	Mixture of boulders, gravel, sand and mud.	High shear strength. Typically, 210–240 kPa
Glaciomarine sediments	Gravelly sandy mud with drop stones.	Moderate shear strength. 15–70 kPa, increasing with depth
Post-glacial mud	Mud derived from reworked glacial sediments	Low shear strength up to 20 kPa.
Post-glacial sand and gravel	Sand and gravel mix derived from reworked glacial sediments	Non-cohesive with cone penetration resistance 5–20 MPa

Post-glacial mud and glaciomarine sediments have low to medium shear strengths, respectively, and occur in relatively thick deposits in the Bay of Fundy (Eamer et al., 2020). The absence of large boulders makes them ideal for monopiles and suction caissons. Analysis is thus performed for OWT caisson foundations installed into glaciomarine sediments, as observed in the Bay of Fundy.

Several studies reported geotechnical properties of glaciomarine sediments in Atlantic and Pacific Canada (e.g., Eamer et al., 2020; MacKillop et al., 2023). The glaciomarine sediments contain primarily silty clay. MacKillop et al. (2023) conducted geotechnical investigation of glaciomarine sediments in Pacific Canada and reported LL = 33–73, PL = 17–35, PI = 11–38, and LI = 1.5–3.0 for this surficial deposit at 35–188 cm depth. A series of triaxial compression tests show $c' = 2.1$ kPa and $\phi' = 33°$ and $s_u/\sigma'_{vo} = 0.29-0.36$. While comprehensive geotechnical properties of soil at these sites at larger depths are not available, there are several studies in the literature where the installation of suction caisson in several offshore environments was modelled (Zhou & Randolph, 2006; Zhou et al., 2023; Wiesenthal & Hanke, 2024). Based on these studies and geotechnical properties reported by Eamer et al. (2020) and MacKillop et al. (2023), the geotechnical properties in Table 2 and loading conditions (e.g., penetration rate) are selected.

2 FINITE ELEMENT MODELLING

The Coupled Eulerian Lagrangian (CEL) approach in Abaqus/Explicit finite element (FE) software is used in the present study. CEL allows for the simulation of large deformation, which uses a fixed background mesh through which the Eulerian material (soil) flows. The material flow is tracked using the Eulerian Volume Fraction (EVF) that varies between 0 and 1, with 1 being fully filled with Eulerian material (soil) and 0 vice versa (void). Abaqus CEL has successfully been used by several researchers to simulate large deformation problems, such as offshore pipeline, landslide, pile installation and other geotechnical problems (Dey et al., 2015; Dutta et al., 2015; Islam et al., 2019; Wang et al., 2022; Karmaker et al., 2024; Staubach et al., 2021; Staubach et al., 2023).

3 CONSTITUTIVE MODEL OF SOIL

The modified Cam clay (MCC) model by Roscoe and Burland (1968) is used to model soil. The MCC model performs well for normally to lightly overconsolidated clays but tends to overestimate

the peak shear strength of highly overconsolidated clays (Mita et al., 2004). The soil in the present study is assumed to be normally consolidated. Unfortunately, the MCC model is not available in Abaqus CEL as a built-in model. Therefore, the MCC model is implemented in CEL by developing a user subroutine VUMAT. The implicit formulations proposed by Borja and Lee (1990) for the integration of the constitutive relations are used with a return mapping based on the closest point projection. This formulation is used because it is simpler to implement since there is no need for yield surface intersection schemes. Also, the plastic stresses do not have to be integrated using a pseudo-time to ensure stability, as is the case in an explicit formulation. These make the implicit formulation of MCC relatively faster in analyses.

Table 2. Geotechnical properties of Glaciomarine sediments used in FE simulation

Parameters	**Value**
For Modified Cam Clay:	
Angle of internal friction, ϕ' (°)	33
Slope of the critical state line in triaxial compression, M_c	1.34
Compression index, λ	0.157
Swelling index, κ	0.015
Initial void ratio, e_0	1.46
Poisson's ratio, ν	0.3
Submerged unit weight, γ (kN/m^3)	10
Coefficient of earth pressure at-rest, K_0	1.0
Permeability (m/s)	1.36 x 10^{-9}
Bulk modulus of air-water mixture, K_m (kN/m^2)	5000

A method proposed by Britto and Gunn (1987) is incorporated in the VUMAT to calculate excess pore water pressure. A stiffness matrix of the soil composite ($\boldsymbol{D}_w$) is defined using the bulk modulus of air-water mixture (K_m) and the soil porosity (n) (Eq. 1). This assumes that the bulk compressibility of the saturated soil is effectively due to the bulk compressibility of the water phase alone, with attention to the volume fraction of the soil occupied by the water (Britto & Gunn, 1987). This simplification implies, the loading produces no change in effective stress and the load is carried by the pore water pressure. Staubach et al. (2021) noted that K_m = 5 MPa gives practical values of excess pore pressure and reasonable computational time. The hydromechanical model is implemented following the algorithm below.

$$\boldsymbol{D}_w = \frac{1}{n}\begin{bmatrix} K_m & K_m & K_m & 0 & 0 & 0 \\ K_m & K_m & K_m & 0 & 0 & 0 \\ K_m & K_m & K_m & 0 & 0 & 0 \\ 0 & 0 & 0 & 0 & 0 & 0 \\ 0 & 0 & 0 & 0 & 0 & 0 \\ 0 & 0 & 0 & 0 & 0 & 0 \end{bmatrix} \quad (1)$$

Algorithm for hydromechanical model implementation

i. Enter the VUMAT with total stresses $\boldsymbol{\sigma}_i$, pore water pressure $\boldsymbol{u}_i$ and total strain increment $\Delta\boldsymbol{\varepsilon}_{i+1}$.
ii. Calculate the effective stresses: $\boldsymbol{\sigma'}_i = \boldsymbol{\sigma}_i - \boldsymbol{u}_i$
iii. Calculate the new pore water pressure: $\boldsymbol{u}_{i+1} = \boldsymbol{u}_i + \boldsymbol{D}_w \Delta\boldsymbol{\varepsilon}_{i+1}$
iv. After elasto-plastic integration to get the new effective stresses $\boldsymbol{\sigma'}_{i+1}$, calculate and return the new total stresses: $\boldsymbol{\sigma}_{i+1} = \boldsymbol{\sigma'}_{i+1} + \boldsymbol{u}_{i+1}$

Where $()_{i+1}$ and $()_i$ refer to quantities at the current time and previous time, respectively. This formulation is appropriate for cases where soil is fully or near full saturation and where the rate of loading is such that there is not enough time for the excess pore pressures to dissipate. The permeability of the glaciomarine sediment is small (Table 2) and the installation occurs fast; therefore, the above method is suitable for the calculation of excess pore water pressure.

4 FINITE ELEMENT MODEL SETUPS

4.1 Material properties and in-situ stress

The initial stress state of the soil is established using the Geostatic stress definition with the water table at 50 m above seabed. The submerged unit weight of the soil is used to define the initial effective stress. The seabed is assumed to be normally consolidated.

4.2 Model geometry, meshing and contact

A suction caisson of internal diameter D = 10 m, length L = 12 m and wall thickness t = 50 mm (e.g., D/200) is considered. In the field, the caisson penetrates at a varying rate depending upon suction and soil resistance at that instant. However, for FE simulation, the caisson is penetrated at constant rate (0.2 m/s). The caisson is modelled as a rigid body by discretizing it with 8-node 3D elements with reduced integration (C3D8R).

Taking advantage of symmetry, the caisson is penetrated at the corner of a one-quarter of the soil domain (20 m radius and 50 m thickness). Also, there is a 0.5 m thick void above this soil domain. That means the vertical boundaries are at 300t far from the caisson surface, and bottom boundary is at 4D from the bottom of the caisson at full penetration. Placing boundaries at such a large distance ensures minimum boundary effects on the solution. Zero velocity boundary conditions normal to the vertical boundaries are applied. All the velocity components are zero at the bottom boundary. In addition, non-reflecting Eulerian boundary conditions are applied to all these boundaries to absorb stress waves hitting them. No boundary condition is applied to the top surface, which allows soil movement near the seabed (e.g., heave and settlement etc.).

The soil and void domains are discretized using 3D hexagonal coupled Eulerian elements with reduced integration (EC3D8R). A structured mesh with finer elements near the caisson and progressively coarser towards the model boundaries is used (Fig. 2a), which reduces computational costs and facilitates gradual damping of the stress waves travelling outward (Staubach et al., 2023). This has been verified by checking the acceleration magnitudes at the model boundaries to be near zero.

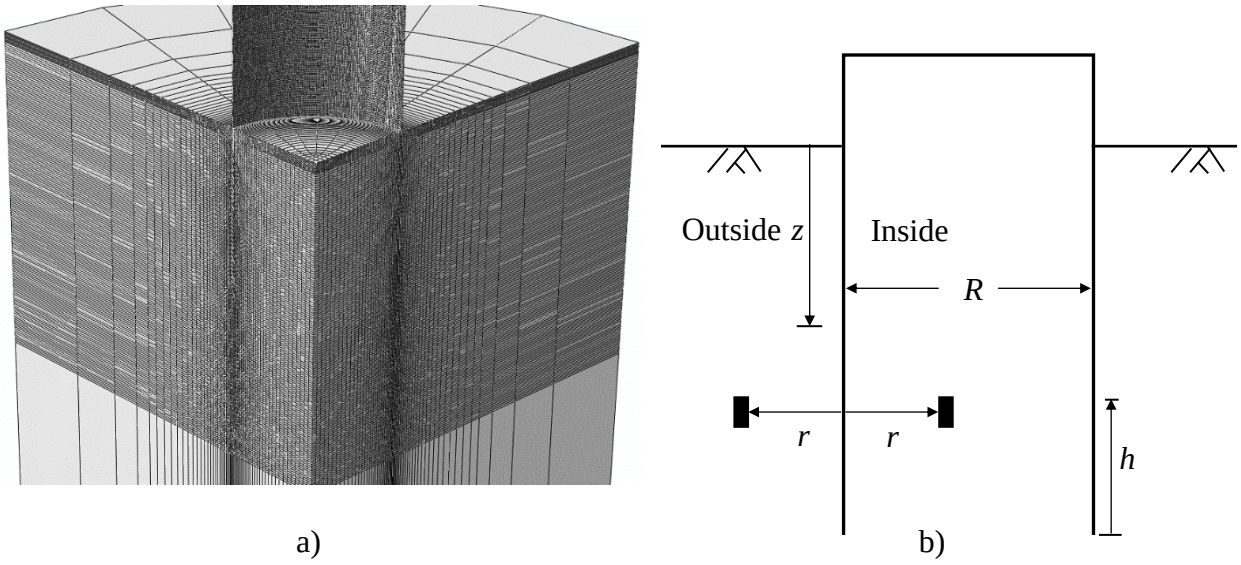

Figure 2. a) Finite element mesh and b) notations used for results

The major notations used in this study are shown in Fig. 2(b). The depth below the seabed is *z*, and the horizontal distance from the caisson wall is *r*. Also, *h* is the vertical distance from the tip of the caisson to a soil element.

The soil-caisson interface resistance plays an important role in the installation of a caisson. The limiting skin friction (τ_s) can be related to local radial effective stress (σ'_r) and soil-caisson interface friction angle (δ) as $\tau_s = \sigma'_r \tan\delta$. Most of the previous studies simulated the penetration in the total stress approach and defined the skin friction as a function of undrained shear strength as $\tau_s = \alpha s_u$, where $0 \leq \alpha \leq 1.0$. On the other hand, in the effective stress approach, as commonly used to calculate the axial capacity of a pile, τ_s is related to vertical effective stress (σ'_v) as $\tau_s = \beta\sigma'_v$ because σ'_v could be estimated more reliably than the radial effective stress. Some studies added an empirical factor to $\beta\sigma'_v$ to take into account installation effects (e.g., densification of sand, Meyerhof, 1976). In the present study, pore water pressure (u) is calculated during large deformation penetration of the caisson. Therefore, the effective radial stress is known. Soil-caisson frictional resistance is defined using the general contact algorithm available in the software. The current version of CEL has been developed for single-phase materials, and the interface resistance can be defined only as a function of total radial stress (σ_r), multiplying it by a friction coefficient (β_t). As the excess pore water pressure is calculated using a user subroutine VUMAT, the effective radial stress can also be calculated ($\sigma'_r = \sigma_r - u$). For each time increment, the ratio of $f_1 = \sigma'_r/\sigma_r$ is calculated for the soil element near the interface. The interface coefficient is then defined as $f_1\beta_t$, which calculates the interface resistance based on local effective radial stress, where β_t represents the soil-caisson interface coefficient ($\tan\delta$). For soil-soil slippage (SS), Azzouz et al. (1990) found that α'_p (effective friction angle at peak shear stress for SS condition) is between 18°–24° for most types of clay. Additionally, early laboratory tests showed that $\alpha'_p - \delta$ does not exceed 5° (Tomlinson, 1971; Littleton, 1976; Lupini, 1981; Martins, 1983; Lemos, 1986). Using the conservative lower limit of α'_p = 18°, δ is 13°, giving $\beta_t = 0.23 \approx 0.2$.

In practice, the suction caisson is penetrated into the seabed by pumping water out of the enclosure. Numerically, this is implemented simply by pushing at a constant velocity of 0.2 m/s to a depth of

10 m. The analyses are performed by maintaining quasi-static conditions. Strain-softening and strain rate effects are not considered.

5 RESULTS

5.1 Material model validation

A consolidated undrained triaxial test performed by MacKillop et al. (2023) for glaciomarine mud is numerically simulated to validate the numerical implementation and performance of the MCC model. The geotechnical properties used in this analysis are shown in Table 2. Figure 3 shows that the numerical analysis is able to reproduce the experimental behaviour of glaciomarine mud with good accuracy.

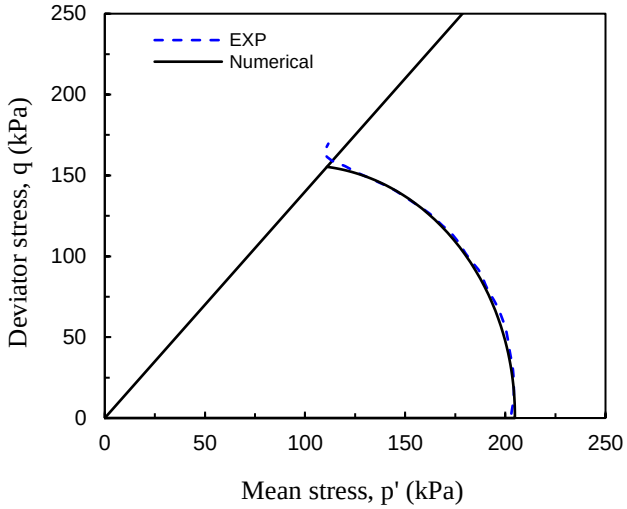

Figure 3. Simulation of a triaxial compression test on glaciomarine mud

5.2 Suction caisson results

During installation of the caisson, a significant increase in total radial stress occurs in the soil elements near the caisson surface. Therefore, in total stress analysis, major attention is given to the total radial stress and is considered the major principal stress (e.g., Lo & Stermac, 1965). The installation of a caisson also increases the excess pore water pressure. As the pore water pressure is calculated in the present study, the installation effects are evaluated using σ'_r/σ_r.

Figures 4(a–d) show the variation of σ'_r/σ_r for four penetration depths (z) of 3 m, 3.2 m, 4 m and 10 m (legend after Fig. 4d also applies to Fig. 4(a–c)). These depths represent z/D = 0.3–1.0 and z/t = 60–200. As installation progresses, σ'_r/σ_r in a region near the wall of the caisson reduces to very small values and almost zero in some elements. This represents very low shear strength in those soil elements. The reduction is more pronounced in elements inside the wall, as shown by a wider zone of reduced effective stress on the right side of each figure in Fig. 4(a–d). This is likely due to the relatively larger flow of soil into the enclosure during installation, which leads to more heave at the ground surface (Fig. 4e). This can be confirmed by the wider pore pressure bulb in the enclosed soil (right side of Fig. 4e).

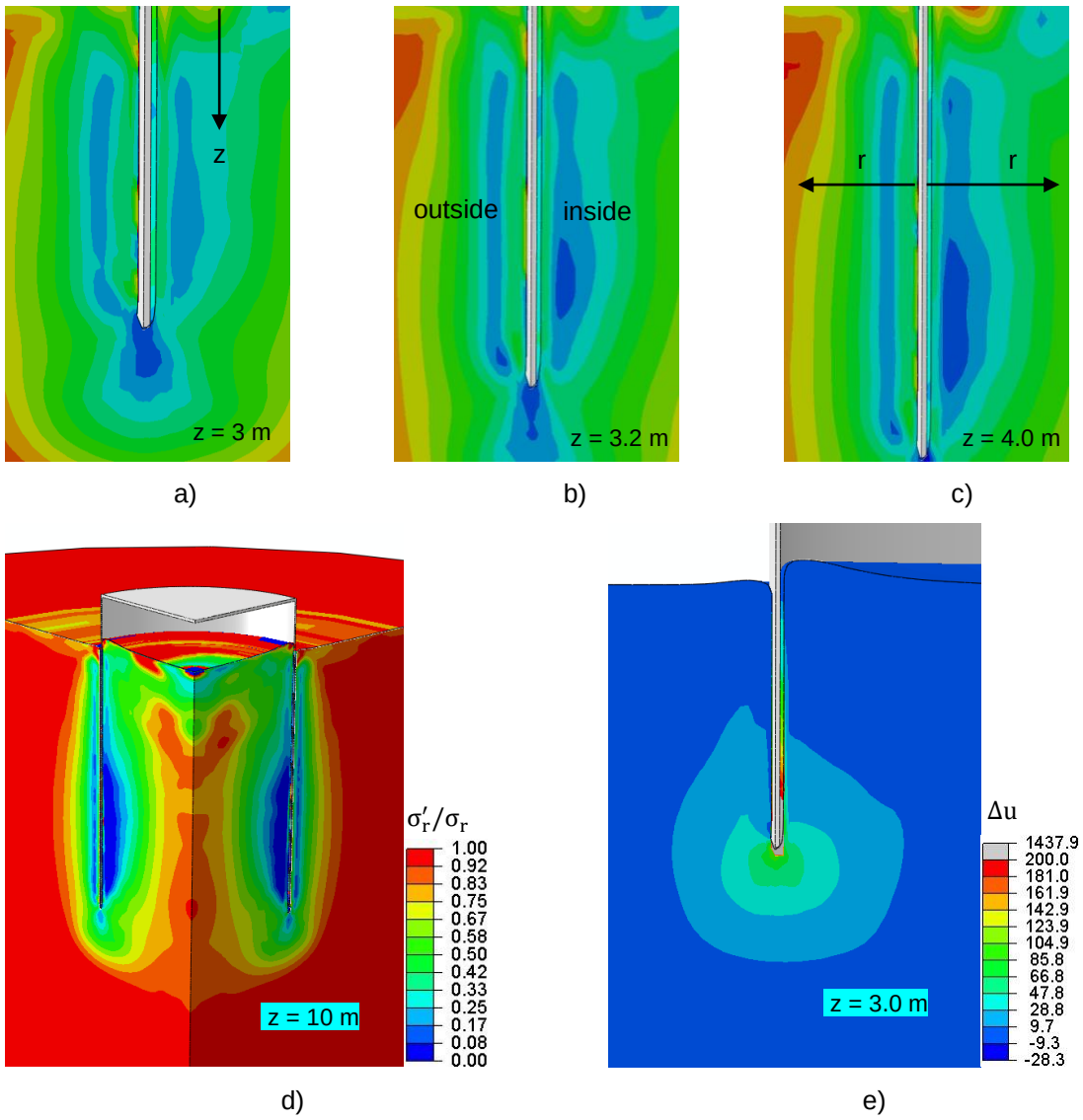

Figure 4. Stress change with installation: (a–d) σ'_r/σ_r ratios at different depths of installation; (e) general excess pore water pressure, Δu

As the initial effective radial stress ($\sigma'_{r0} = K_0\gamma' z$) and pore water pressure ($u_0 = \gamma_w z$) are depth dependent, the development of radial stress and pore water pressure due to installation is further examined by normalizing them with the initial values as σ'_r/σ'_{r0} and u/u_0. Figure 5(a) shows the variation of σ_r/σ'_{r0} and σ'_r/σ'_{r0} with radial distance (r) measured from the face of the caisson wall. Again, the right side of these figures represent the inner part of the caisson. When the caisson penetrates to the depth (z) of interest (h/R = 0), σ_r increases significantly on both sides of the caisson wall. The radial effective stress σ'_r/σ'_{r0} also increases; however, the increase is not as significant as the total stress. In other words, the total stress increase mainly generates pore water pressure as shown in Fig. 5(b).

All three stresses (σ_r, σ'_r and u) reduce with further penetration of the caisson (e.g., h/R = 0.04 and h/R = 0.2), which is due to unloading of the soil elements. The total stress and pore water pressure

reduce towards the in-situ state while the effective radial stress reduces to very small values, especially near the caisson wall. The reduction of σ'_r is higher in soil elements inside the caisson and becomes almost zero in some soil elements. The reduction of σ'_r occurs over a larger radial distance inside the caisson (~up to 0.6R) than the soil elements outside the caisson (0.4R).

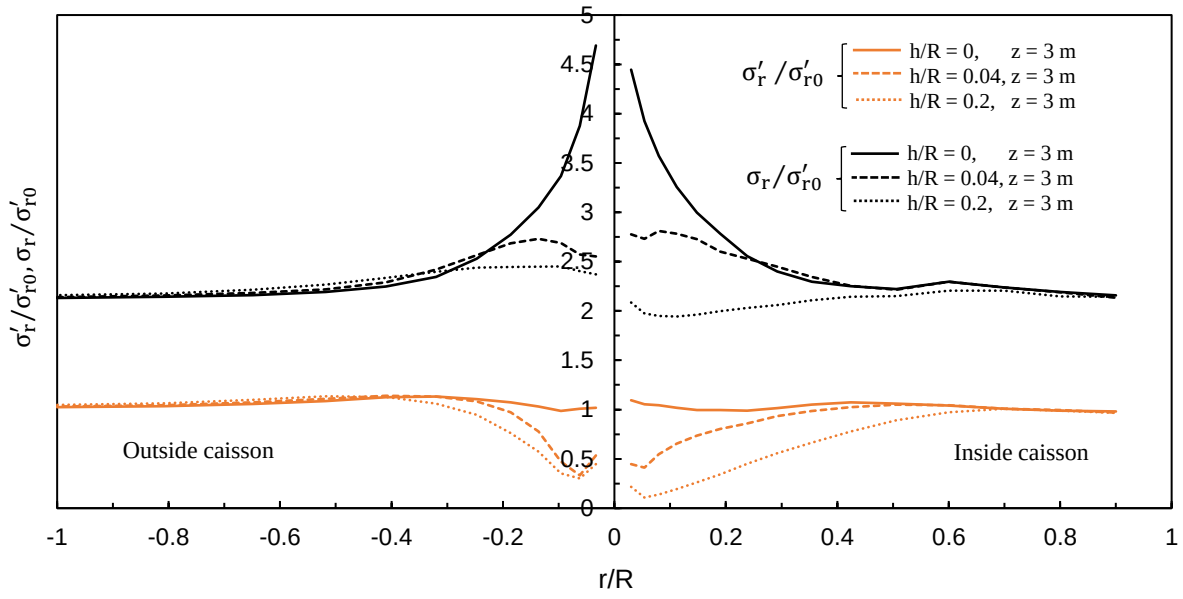

a)

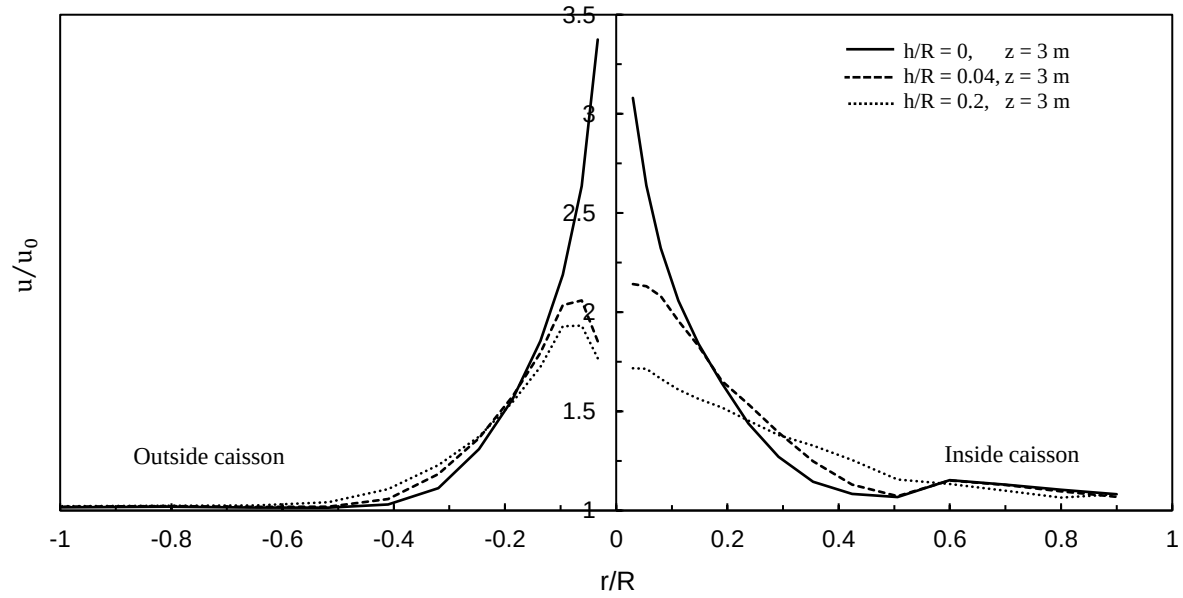

b)

Figure 5. Plots for a) normalised effective stresses, σ'_r/σ'_{r0} and total radial stresses, σ_r/σ'_{r0} and b) normalised pore water pressure, u/u_0 at depth of 3 m for different *h/R* positions against normalised radial distance r/R from caisson wall

Figure 5 also shows that, the change in radial stresses and pore water pressure in the soil elements outside the caisson is relatively small when the caisson tip moves from h/R = 0.04 to h/R = 0.2. However, it is significant for the soil elements inside the caisson. This is likely a result of a relatively higher flow of soil into the enclosure during installation. This means that the σ'_r in the enclosed soils near the wall will reach a steady state only when the caisson tip is far past the depth of interest such that further soil flow during installation has little influence on soils at the depth of interest (see Fig. 5a).

The normalised effective radial stress and normalised pore water pressure at a radial distance of 0.25 m (r/R = 0.05, near caisson wall) is tracked for soil element at depth of 3 m on both sides of the caisson wall during installation (Fig. 7). The normalized negative values in Fig. 7 are simply for ease of plotting and should be read as positive. The peak values represent times when the caisson tip is at the depth of interest, 3 m.

As the caisson approaches the 3 m depth, the σ'_r reduces initially and is lowest at about 0.5 m above the depth of interest (Fig. 7a). This is because, as the caisson approaches, $S_z > S_r$ ($\Delta\varepsilon_z > \Delta\varepsilon_r, \Delta\varepsilon_\theta$) which causes the soil to be compressed in the z direction (positive ε_z) and to elongate in the r and θ directions (negative ε_r, ε_θ) (where S_z, S_r is the applied stress from caisson in the vertical and radial directions respectively on the soil element and $\Delta\varepsilon_r, \Delta\varepsilon_z, \Delta\varepsilon_\theta$ are strain increments in the respective directions) (Fig. 6). This elongation causes a reduction in the σ'_r to about 40% its initial value.

As the caisson further approaches the 3 m depth of interest (from z > 2.5 m), there is a point where $S_z < S_r$ ($\Delta\varepsilon_z < \Delta\varepsilon_r, \Delta\varepsilon_\theta$) as more of the load is applied radially. This causes the soil to be compressed in the r and θ directions (+ ε_r, ε_θ) and to elongate in the z direction (- ε_z) (Fig. 6). This leads to an increase in the σ'_r to a peak when $S_z = 0$ and the caisson is at 3 m depth so that, the load from the caisson is fully applied as a radial stress on the soil element (Fig. 7a). During this process, the elongation and compression of the soil element induces volumetric strain changes ($\Delta\varepsilon_v$) that cause excess pore pressures (Δu) to generate. The u increases gradually to a peak (Fig. 7b) when the caisson is at 3 m depth. This is because the $\Delta\varepsilon_v = \Delta\varepsilon_z + \Delta\varepsilon_r + \Delta\varepsilon_\theta$ for the soil undergoing elongation and compression up to this point is positive (Fig. 6). As the caisson passes the 3 m depth, the applied radial stress from the caisson begins to unload, causing σ'_r to reduce. This leads to a reduction in ε_r (- $\Delta\varepsilon_r$). At the same time, the soil being pushed upwards by the caisson as it passes the 3 m depth, applies a compressive load (+$\Delta\varepsilon_z$) from below, on soils at the 3 m level. This leads to an increase in ε_z (Fig. 6). This process causes the $\Delta\varepsilon_v$ to become negative which causes a reduction in the pore water pressure ($\Delta\varepsilon_\theta \approx 0$, $\Delta\varepsilon_r < 0$, $\Delta\varepsilon_z > 0$ and $\Delta\varepsilon_r < \Delta\varepsilon_z$, Fig. 6). This unloading continuous to a point (about 0.6 m past the 3 m depth) where the caisson effect becomes negligible and $\Delta\varepsilon_v = 0$ ($\Delta\varepsilon_r = \Delta\varepsilon_\theta, = \Delta\varepsilon_z \approx 0$). The u and σ'_r become almost constant after this point.

The influence of soil flow on σ'_r and u can be inferred from the total strains plot in Fig. 6. As the caisson moves towards the 3 m depth (up to 2.5 m), soils in the caisson and outside have similar magnitudes of deformations for any given strain, $\varepsilon_r, \varepsilon_z, \varepsilon_\theta$. Past the 2.5 m point, the soil in the caisson and the soil outside experience different magnitudes of deformation for any given strain. Between the enclosed soil and outside soil, ε_r is the largest in the enclosed soil, likewise for ε_z, ε_θ. This is due to the relatively higher flow of soil into the caisson as it is installed. Also σ'_r near the wall reduces more gradually to near zero on the inside, as opposed to the outside where the

decrease in σ'_r is relatively rapid and non-zero (notice the rate of reduction in strains for soil inside and outside the caisson in Fig. 6).

The normalized effective stress path (ESP) and total stress path (TSP) for the point tracked on the inside of the caisson in Fig. 7 are plotted in Fig. 8a. The ESP approaches the critical state line (CSL) with reducing p'/p_c and increasing q/p_c. The TSP increases vertically before moving rightward with increasing p'/p_c and q/p_c. The movement of the ESP and TSP in opposite directions is due to increasing pore water pressure.

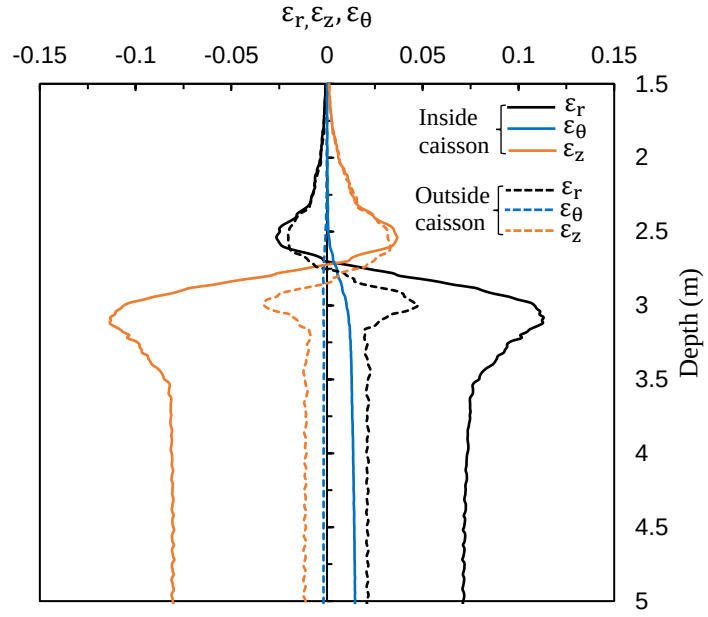

Figure 6. Plot of ε_r, ε_θ ε_z for soil inside and outside the caisson at r = 0.25 m against caisson position during installation

The point where the ESP touches the CSL is when the caisson is at the 3 m depth. This shows that the soils in the immediate vicinity of the caisson are completely loaded to critical state as it is installed. As the caisson continues past 3 m depth, the ESP and TSP begin to unload with reducing $p'/p_c, p/p_c$ and reducing q/p_c. The TSP unloads along approximately same path it loaded while the ESP unloads approximately unloads parallel to the CSL. As the caisson goes deeper such that its influence on the soil element being measured is insignificant, the ESP and TSP stop. The TSP settles around $p = 1.05p_c$ showing that the total mean stresses in the soil before caisson installation are relatively unchanged after installation. However, the effective stress at the end reduces significantly from the initial value to $p' = 1.05p_c$. This implies significant pore pressure generation due to installation. Figure 8b shows the installation force to be increasing with installation depth.

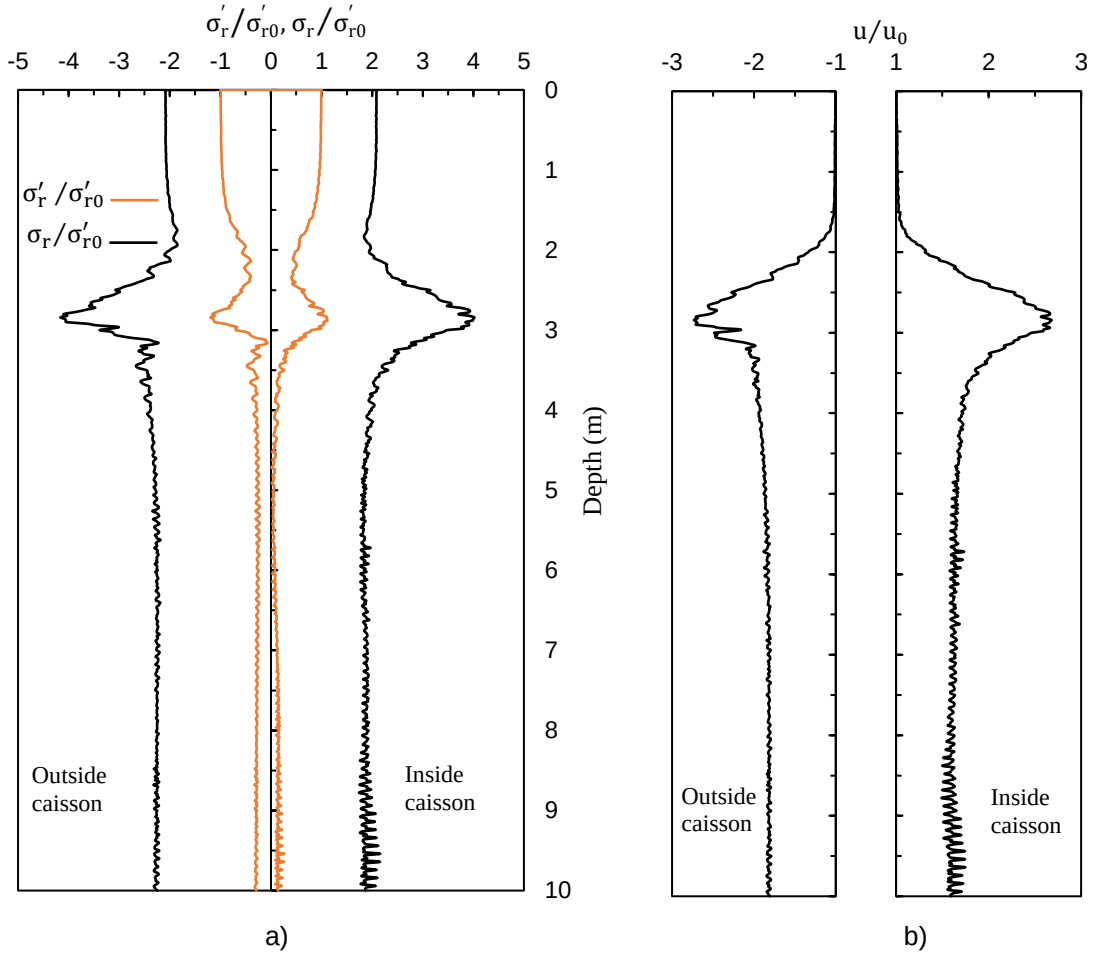

Figure 7. (a) normalised effective and total radial stresses, (b) normalised pore water pressure in a soil element at depth of 3 m and radial distance of 0.25 m from caission surface.

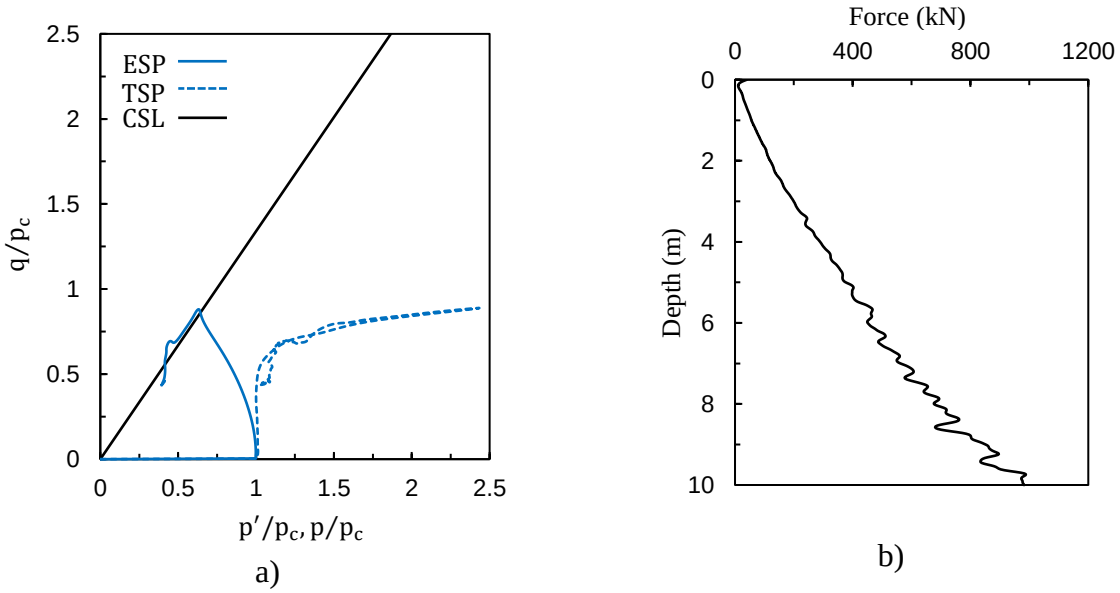

Figure 8. (a) Stress paths of soil element at depth of 3 m and radial distance of 0.25 m; (b) Jacking force

6 CONCLUSIONS

An effective stress based method using the modified Cam clay model, coupled with a simple hydromechanical formulation for calculating excess pore pressures, is used to perform numerical analysis for installation of potential suction caisson foundations for offshore wind turbines in glaciomarine sediment in Atlantic Canada. Using this approach, the effective stresses and pore water pressure behavior with radial distances and depth for soil elements inside and outside the foundation are studied. The influence of soil flow on developed stresses and pore water pressure is examined based on the changes in strain components during installation. The effective radial stress close to the foundation walls could be very small or near zero, which could give low caisson–soil interface resistance during installation. The total radial stress in soil elements near the caisson increases significantly when the caisson tip reaches close to it. On the other hand, the effective stress in those soil element reduces and remains very small even when the tip penetrates further deep, which means significant pore pressure generation. Subsequent dissipation of this pore pressure will affect the pullout capacity of the caisson.

REFERENCES

Archer, C.L. & Jacobson, M.Z., 2005. Evaluation of global wind power. *Journal of Geophysical research: Atmospheres,* 110(D12).

Azzouz, A.S., Baligh, M.M. & Whittle, A.J., 1990. Shaft resistance of piles in clay. *Journal of Geotechnical Engineering,* 116(2), pp.205–221.

Blue, R. & Jeyakumar, B., 2022. *Offshore wind in Canada,* s.l.: PEMBINA institute.

Borja, R.I. & Lee, S.R., 1990. Cam clay plasticity, part I: Implicit integration of elasto-plastic constitutive relations. *Computer methods in applied mechanics and engineering,* pp.49–72.

Britto, A. M. & Gunn, M. J., 1987. *Critical state soil mechanics via finite elements.* New york: Ellis Horwood limited.

Cao, J. et al., 2002. Excess pore pressures induced by installation of suction caissons in NC clays. In: Offshore Site Investigation and Geotechnics: Diversity and Sustainability, *Proceedings of the 5th international conference.*

Dey, R., Hawlader, B., Philips, R. & Soga, K., 2015. Large deformation finite element modeling of progressive failure leading to spread in sensitive clay slopes. *Géotechnique,* 65(8), pp.657–668.

Dutta, S., Hawlader, B. & Phillips, R., 2015. Finite element modeling of partially embedded pipelines in clay seabed using Coupled Eulerian–Lagrangian method. *Canadian Geotechnical Journal,* 52(1), pp.58–72.

Eamer, B.J., Shaw, J., King, E.L. & MacKillop, K., 2021. The inner shelf geology of Atlantic Canada compared with the North Sea and Atlantic United States: Insights for Atlantic Canadian offshore wind energy. *Continental Shelf Research,* 213(104297) pp.104–297.

Eamer, B.J., Shaw, J., King, E.L. & MacKillop, K., 2020. *Seabed conditions on the inner shelves of Atlantic Canada;* Geological Survey of Canada, Open file 8731.

Houlsby, G.T. & Byrne, B.W., 2005. Design procedures for installation of suction caissons in clay and other materials. In: *Proceedings of the Institution of Civil Engineers*, pp. 75-82.

Islam, N., Hawlader, B., Wang, C. & Soga, K., 2019. Large-deformation finite-element modelling of earthquake-induced landslides considering strain-softnening behaviour of sensitive clay. *Canadian Geotechnical Journal,* Volume 56, pp.1003–1018.

Karmaker, R., Hawlader, B., Perret, D. & Dey, R., 2024. Numerical modelling of pile jacking in highly sensitive clays. *Canadian Geotechnical Journal,* 61(12), pp.2597–2614.

Kopp, D.R., 2010. *Foundations for an offshore wind turbine,* M.Eng. Massachusetts: Massachusetts Institute of Technology.

Leblanc, C., Houlsby, G. & Byrne, B., 2010. Response of stiff piles in sand to long-term cyclic lateral loading. *Géotechnique,* pp.79–90.

Lemos, L.J., 1986. *The effects of rate on the residual strength of soil,* PhD. London: Imperial College, London University.

Littleton, I., 1976. An experimental study of the adhesion between clay and steel. *Journal of Terramechanics,* 13(3), pp.141–152.

Lo, K. Y. & Stermac, A. G., 1965. Induced pore pressures during pile-driving operations. In: *Proceedings of the 6th International Conference on Soil Mechanics and Foundation Engineering*, Montréal.

Lupini, J.F., 1981. *The residual strength of soils,* PhD. London: Imperial College, London University.

MacKillop, K., Eamer, J. B. & Greaves, C., 2023. *Geotechnical characteristics of near-surface or surficially exposed glaciomarine sediments on the inner shelf of pacific Canada, British Columbia,* Geological Survey of Canada, Open file 8953, 1 poster.

Martins, J. P., 1983. *Shaft resistance of axially loaded piles in clay,* PhD. London: Imperial College, London University.

Meyerhof, G.G., 1976. Bearing capacity and settlement of pile foundations. *Journal of the Geotechnical Engineering Division,* 102(3), pp.197–228.

Mita, K.A., Dasari, G.R. & Lo, K.W., 2004. Performance of a three-dimensional hvorslev-modified Cam clay model for overconsolidated clay. *International Journal of Geomechanics,* 4(4), pp.296-309.

Department of Energy (DOE), 2023. *Offshore Wind Market Report:2023 Edition,* US: DOE.

Roscoe, K. H. & Burland, J. B., 1968. On the generalised stress-strain behaviour of wet clays.. *Engineering Plasticity. Cambridge university press,* pp. 535-609.

Shaw, J. et al., 2006. A conceptual model of the deglaciation of Atlantic Canada. *Quaternary Science Reviews,* 25(17–18), pp.2059–2081.

Staubach, P., Machacek, J., Skowronek, J. & Wichtmann, T., 2021. Vibratory pile driving in water-saturated sand: Back-analysis of model tests using a hydro-mechanically coupled CEL method. *Soils and Foundations*, 61(1), pp.144–159.

Staubach, P., Tschirschky, L., Machacek, J. & Wichtmann, T., 2023. Monopile installation in clay and subsequent response to millions of lateral load cycles. *Computers and Geotechnics*, 155, pp. 105–221.

CanmetENERGY, 2021. *Offshore Wind Technology Scan*, Ottawa: Natural Resources Canada, Renewable and Electrical Energy Division.

Tomlinson, M. J., 1971. Adhesion of piles driven in clay soils. In: *Proceedings of the 4th International Conference on Soil Mechanics and Foundation Engineering*, pp.66–71.

Wang, C., Hawlader, B., Perret, D. & Soga, K., 2022. Effects of geometry and soil properties on type and retrogression of landslides in sensitive clays. *Géotechnique*, 72(4), pp.322–336.

Wiesenthal, P. & Henke, S., 2024. Concept of plug development in jacked open-ended piles in clay considering total stresses. Acta Geotechnica, Volume 20, pp.1019–1033.

Zhou, H. & Randolph, M. F., 2006. Large deformation analysis of suction caisson installation in clay. Canadian Geotechnical Journal, 43(12), pp.1344–1357.

Zhou, S., Zhou, M., Zhang, X. & Tian, Y., 2021. Installation of caisson in non-uniform clay interbedded with a sand layer. Computers and Geotechnics, Volume 140, pp.104–439.